International Journal of Heat and Mass Transfer 110 (2017) 422–436

Contents lists available at ScienceDirect

International Journal of Heat and Mass Transfer

journal homepage: www.elsevier.com/locate/ijhmt

Flow boiling heat transfer of R134a in multi microchannels

E.M. Fayyadh [a], M.M. Mahmoud [b,c], K. Sefiane [d], T.G. Karayiannis [b,*]

[a] University of Technology, Department of Mechanical Engineering, 10066 Alsina'a Street, Baghdad, Iraq
[b] Brunel University London, College of Engineering, Design and Physical Sciences, Kingston Lane, Uxbridge, Middlesex, London UB8 3PH, UK
[c] Faculty of Engineering, Zagazig University, Zagazig 44519, Egypt
[d] School of Engineering, The University of Edinburgh, Kings Buildings, Mayfield Road, Edinburgh EH9 3JL, UK

ARTICLE INFO

Article history:
Received 22 August 2016
Received in revised form 16 March 2017
Accepted 17 March 2017
Available online 24 March 2017

Keywords:
Microchannel
Flow boiling
Flow patterns
Heat transfer rates

ABSTRACT

Experiments were conducted to investigate flow boiling heat transfer of R134a in a multi microchannel heat sink. The heat sink consisted of 25 rectangular microchannels with nominal dimensions of 300 μm wide, 700 μm deep (D_h = 420 μm) and 200 μm separating wall thickness. The heat sink was made of oxygen free copper by CNC machining and was 20 mm long and 15 mm wide. The experiments were conducted at 6.5 bar system pressure and covered a footprint area-based heat flux range 11.46–403.1 kW/m^2 and mass flux range 50–300 kg/m^2 s. A high speed camera was used to capture the flow patterns simultaneously with heat transfer measurements. Three flow patterns were observed namely bubbly, slug and wavy-annular flow when the heat flux increased gradually. The heat transfer coefficient increased with heat flux and there was no mass flux effect. Assessing existing correlations indicated that the correlations of Mahmoud and Karayiannis (2013) and Cooper (1984) predict the data very well with a mean absolute error less than 20% compared to the other correlations.

1. Introduction

Two phase flow boiling microchannel heat sinks have emerged as one of the most effective solutions for cooling high and ultra-high heat flux devices such as electronics systems. In addition, Mudawar [1] reported that the applications of two phase microchannel heat sinks is not limited only to electronics cooling. He discussed and summarized other possible applications which include: (1) cooling turbine blades, (2) cooling fusion reactor blankets, (3) cooling the nozzles of rocket engines, (4) cooling power electronics in avionics and hybrid vehicles, (5) cooling hydrogen storage reservoirs, (6) refrigeration cooling, and (7) thermal control in microgravity and capillary–pumped loops. Despite this wide range of applications, two phase microchannel heat sinks are still not commercially available. This arises from the fact that many fundamental issues in flow boiling at microscale are still to be elucidated, e.g. flow instabilities, dominant heat transfer mechanism (s), critical heat flux and lack of generally accepted design correlations. Research conducted in this area in the last two decades did not reach comprehensive and universal conclusions about these issues. Table 1 summarizes some of the previous experimental studies that are relevant to mini/microchannels and the experimental conditions covered in these studies. They demonstrate that there is no common agreement on the dominant heat transfer mechanism(s). For instance, one group of researchers such as [2–6] concluded that nucleate boiling is the dominant heat transfer mechanism. A second group, [7–9], reported that convective boiling is the dominant heat transfer mechanism. A third group, [10–13], reported that nucleate boiling mechanism dominates at low vapour quality, while convective boiling mechanism dominates at high qualities. These studies used conventional criteria to infer the dominant heat transfer mechanism, i.e. heat transfer coefficient depends only on vapour quality and mass flux in convective boiling while it depends only on heat flux in nucleate boiling. This discrepancy among research groups in terms of flow patterns, heat transfer mechanisms and rates may be attributed to the difference in experimental conditions, channel size, length, material and surface finish, see Karayiannis et al. [14].

Some researchers conducted flow visualization simultaneously with heat transfer measurements in order to understand the prevailing heat transfer mechanism(s). For example, Chen and Garimella [2] conducted a flow visualization study for flow boiling of FC-77 inside a silicon-based multi microchannel heat sink. The location of the high speed camera was at the centre of the heat sink. At low heat fluxes, small bubbles were observed to nucleate

* Corresponding author at: College of Engineering, Design and Physical Sciences, Brunel University London, Uxbridge, Middlesex, UB8 3PH, UK.
E-mail addresses: ikhlase60@yahoo.com (E.M. Fayyadh), mohamed.mahmoud@brunel.ac.uk, mbasuny@zu.edu.eg (M.M. Mahmoud), k.sefiane@ed.ac.uk (K. Sefiane), tassos.karayiannis@brunel.ac.uk (T.G. Karayiannis).

http://dx.doi.org/10.1016/j.ijheatmasstransfer.2017.03.057
0017-9310/

Nomenclature

c_{pf}	liquid specific heat [J/kg]
C'	constant in Eq. (15)
d	vertical distance between the thermocouple and the channel bottom
D_b	bubble departure diameter [m]
D_{eq}	equivalent bubble diameter [m]
D_h	hydraulic diameter [m]
f_{exp}	experimental fanning friction factor [–]
f_{sp}	single phase Fanning friction factor [–]
g	gravitational acceleration [m/s^2]
G	mass flux [kg/m^2 s]
h	heat transfer coefficient [W/m^2 K]
h_{fg}	latent heat [J/kg]
h_{exp}	experimental heat transfer coefficient [W/m^2 K]
H_{pred}	predicted heat transfer coefficient [W/m^2 K]
H_{ch}	channel height [m]
i	specific enthalpy [kJ/kg]
i_f	specific enthalpy of saturated liquid [kJ/kg]
i_g	specific enthalpy of saturated vapour [kJ/kg]
i_{exit}	specific enthalpy at the exit pressure and temperature [kJ/kg]
Ja	Jacob number [–], see Eq. (25)
K_{mi}	inlet manifold loss coefficient [–]
K_{mo}	outlet manifold loss coefficient [–]
k_c	copper thermal conductivity [W/m K]
k_f	liquid thermal conductivity [W/m K]
$K(\infty)$	constant in Eq. (14)
L	channel length [m]
L_{ba}	length of the axis of the bubble in the axial direction [m]
L_{bt}	length of the axis of the bubble in the transvers direction [m]
L_{sp}	single phase length [m]
m	fin parameter, $\sqrt{2h/k_cW_{th}}$
M	molecular mass [kg/kmol]
$\dot{m}$	mass flow rate [kg/s]
N	number of channels, number of data points
Nu	Nusselt number [–]
P_R	reduced pressure [–]
Pr	Prandtl number [–]
ΔP	pressure drop [Pa]
Δp_{ch}	channel pressure drop [Pa]
Δp_{sc}	pressure drop due to sudden contraction [Pa]
Δp_{ex}	pressure drop due to sudden expansion [Pa]
Δp_{loss}	pressure losses [Pa]
Δp_{mi}	pressure drop in the inlet manifold [Pa]
Δp_{mo}	pressure drop in the outlet manifold [Pa]
Δp_m	measured pressure drop [Pa]
Δp_{sp}	single phase pressure drop [Pa]
Δp_{tp}	two phase pressure drop [Pa]
q''	base heat flux [W/m^2]
R_p	surface roughness [m]
Re	Reynolds number (GD_h/μ_f) [–]
t_d	bubble departure time [s]
t_w	bubble waiting time [s]
T	temperature [K]
$T_{f,in}$	fluid inlet temperature [K]
T_f	fluid temperature [K]
T_{sat}	saturation temperature [K]
T_{th}	thermocouple reading [K]
T_w	channel inner wall temperature [K]
$T_{w,m}$	wall temperature at mid location [K]
v_f	specific volume of saturated liquid [m^3/kg]
v_g	specific volume of saturated vapour [m^3/kg]
W	heat sink width [m]
W_{ch}	channel width [m]
We_l	liquid Weber number [–]
W_{th}	channel separating wall thickness [m]
x	vapour quality [–]
x_{mid}	vapour quality at mid location [–]
x_{exit}	exit quality [–]
x^+	dimensionless axial distance, L/ReD_h [–]
y	vertical distance [m]
z	axial distance [m]

Greek symbols

β	aspect ratio or Small to large cross sectional area ratio, ±30% error band
θ	diffuser/nozzle conical angle [°]
η	fin efficiency [–]
μ_f	liquid viscosity [Pa s]
ρ_f	liquid density [kg/m^3]
ρ_g	vapour density [kg/m^3]
σ	surface tension [N/m]

Table 1
Summary of prior studies relevant to parallel rectangular multi mini/microchannels.

Author	Material	D_h [mm]/L[mm]/No. of channels	Fluid/T_{in} [°C]/T_{sat} [°C]/P_{in} [bar]	G [kg/m^2 s]	q″ [kW/m^2]
Agostini et al. [8]	Copper	0.336/20/67	R236fa/–/25/2.73	281–1501	36–2210
Balasubramanian et al. [13]	Copper	0.504–0.4887/25, 20/40,16	Water/90/–/–	88–751	Up to 4200
Bertsch et al. [3]	Copper	1.090/9.53/17	R134a/–/8.9–29/4–7.5	20.3–81	Up to 200
Bertsch et al. [4]	Copper	1.090–0.54/9.53/17, 33	R134a, R245fa/–/8–30/-	20–350	Up to 220
Chen and Garimella [2]	Silicon	0.389/12.7/24	FC-77/71/–/–	267–458	40–800
Harirchian and Garimella [11]	Silicon	0.16–0.749/12.7/2–60	FC-77 /92/–/–	250–1600	Up to 4000
Harirchian and Garimella [15]	Silicon	0.16–0.749/12.7/2–60	FC-77 /92/–/–	225–1461	Up to 3500
Leao et al. [6]	Copper	0.167/15/50	R407C/ΔT_{sub} = 5–15/–	400–1500	Up to 310
Lee and Garimella [12]	Silicon	0.16–0.538/12.7/10–60	Water/90–95.1/–/–	46–126	100–3400
Lee and Mudawar[10]	Copper	0.349/25.3/53	R134a/–/–/1.44–6.6	127–654	159–938
Madhour et al.[5]	Copper	0.174./15/100	R134a/–/63/–	205–1000	25.7–1890
Mortada et al.[9]	Aluminium	1.1/300/6	R1234yf, R134a/–/–/7.7	20–100	2–15
Qu and Mudawar [7]	Copper	0.349/44/21	Water/30–60/–/1.17	135–402	400–,300,879–2400

D_h is hydraulic diameter, L is channel length, T_{in} is fluid inlet temperature, T_{sat} is saturation temperature, P_{in} is inlet pressure, G is mass flux, q" is heat flux.

on the channel walls then grow, detach and move downstream with a little chance of coalescence. As heat flux was increased, bubble growth and coalescence rates increased resulting in confined bubbles and slug flow. The slug flow was sustained over a narrow range of heat flux. With further increase in heat flux, alternating churn and wispy-annular flows were observed and continued until dryout occurred. It is interesting to note that when the camera was moved to the upstream side near the channel inlet, flow reversal

was observed at the heat flux value corresponding to the occurrence of alternating churn and wispy-annular flow. In other words, this alternating flow occurs due to flow reversal, [2]. Harirchian and Garimella [15] investigated the effect of channel width and mass flux on flow boiling patterns using FC-77 as the working fluid. They reported five flow patterns, namely: bubbly, slug, churn, wispy-annular and annular flows. The flow patterns observed in channels of width 0.1 and 0.25 mm were found to be similar but different from those observed in the channels of width ≥0.4 mm. The difference is that bubbly flow was suppressed in the channels of small width and instead, slug flow developed immediately after boiling incipience. With increasing heat flux, intermittent churn/annular flow occurred. By contrast, in the channels of large width, bubbly and intermittent churn/wispy annular flows were observed. Accordingly, Harirchian and Garimella [15] concluded that nucleate boiling dominates in channels of width ≥0.4 mm, while convective boiling dominates in channels of smaller width.

The above review demonstrates that more research is still required in order to understand the flow boiling heat transfer characteristics and mechanism(s) in microchannels. Therefore, one of the main objectives of the present work was to carry out flow visualization studies simultaneously with heat transfer measurements to record and help elucidate prevailing flow patterns and related heat transfer rates. At the same time flow instability and reversal were to be studied. The working fluid was R134a and the channel had a 0.42 mm hydraulic diameter. As mentioned above, validated correlations are needed for the wide use of multichannel heat sinks in cooling high heat flux devices. Therefore, the results of this experimental study were used to assess proposed correlations predicting heat transfer rates.

2. Experimental setup

2.1. Flow loop

The experimental facility consists of two closed loops. The first one is the test loop using R134a refrigerant while the second is an auxiliary cooling loop using R404a. Fig. 1 shows a schematic diagram of the test loop including a close-up photograph of the test section part. It consists of R134a tank, a gear pump, a sub-cooler, two Coriolis flow meters with an accuracy of ±0.1% (one for low flow rate (20–100 kg/h) and the other for high flow rate (100–350 kg/h)), a pre-heater, the test section and a condenser. The system includes two inline filters of 25 μm size and three sight glasses in the upstream side of the test section, which were used to confirm that there is no boiling in the pre-heater. System pressure was kept constant by controlling the R134a tank temperature using an immersion heater controlled by a PID controller.

2.2. Test section

Fig. 2 depicts the details of the test section. It consists of an oxygen free copper block with microchannels on its top surface, polycarbonate housing, polycarbonate and quartz glass top cover plates (not shown in the figure) and cartridge heaters. Twenty-five rectangular microchannels were cut into the top surface of the oxygen free copper block using a CNC machine with a feed rate of 550 mm/min. The copper block has overall dimensions of 15 mm width, 20 mm length, i.e. (20×15 mm^2 as a base area) and 74 mm height (64 + 10 mm, see Fig. 2(c)). The nominal dimensions of the microchannel, see Fig. 2(b), are 0.3 mm width (W_{ch}), 0.7 mm depth (H_{ch}), 0.2 mm separating wall thickness (W_{th}) and 20 mm length (L). These dimensions were measured using an electron microscope and the actual values are 0.297 mm in width, 0.695 mm in height and, the separating wall was 0.209 mm thick. The surface roughness was measured using a Zygo NewView 5000 surface profiler. For roughness measurements, three channels were cut on a slice of oxygen free copper using the CNC machine with the same feed rate as for the test section. This was done because the size of the test section (copper block) was larger than the allocated space in the Zygo instrument. The surface roughness of the bottom wall was measured and the *Ra* value was 0.301 μm. This value was the average of measurements at three axial locations for each channel. It was difficult to measure the surface roughness of the side walls. Note that the feed rate of the cutting tool (550 mm/min in this case) can affect the resulting surface roughness. Three cartridge heaters of 175 W heating power each were inserted horizontally at the bottom of the copper block to provide the heating power to the test section, see Fig. 2(a). The power was controlled by a variac and measured by a power meter Hameg HM8115-2 with accuracy of ±0.4% for both current and voltage. Six T-type thermocouples were inserted vertically along the centreline of the copper block at 12 mm equidistance to measure the heat flux. Three T-type thermocouples were inserted along the axial direction of the channel at 8 mm equidistance and 1 mm from the channel bottom to help measure the local heat transfer coefficient along the channel. Another row of thermocouples parallel to these three thermocouples and spaced by 12 mm vertical distance were used to help verify that there is no heat flow in the horizontal direction (direction of flow), see Fig. 2(c), i.e. the test section was adequately insulated. All thermocouples were 0.5 mm diameter and inserted at the centre plane of the copper block. These thermocouples were calibrated with an accuracy of ±0.3 K. The copper block was inserted into the polycarbonate housing and was sealed using two O-rings as seen in Fig. 2. The housing consists of the inlet/outlet plenums and manifolds. The fluid inlet and outlet temperature were measured using T-type thermocouples of 1 mm diameter, which were calibrated with an accuracy of ±0.5 K. The fluid inlet and outlet pressure were measured using absolute pressure transducers located immediately before and after the test section. These transducers were calibrated with an accuracy of ±0.15% and ±0.32% for inlet and outlet respectively. Pressure drop was measured directly across the test section using a calibrated differential pressure transducer (PX771A100DI) with an accuracy of ±0.081%. The depth of the inlet/outlet manifold is the same as the depth of the microchannel. A number of holes (0.7 mm) were drilled into the housing to pass the thermocouples wires through them. A transparent layer of quartz glass with 8 mm thickness was sandwiched between the upper surface of the housing and the top polycarbonate cover plate. This layer was sealed using O-ring embedded in the top surface of the housing. The top cover plate has a visualization window of similar dimension as the microchannels including the manifolds. Flow visualization was conducted using a high speed camera Phantom V.6 with 1000 f/s at full resolution 512×512 pixels. The field of view at this setting was 4 mm × 4 mm. The camera was integrated with a microscope for better flow visualization. The data were recorded using IMP35951 data acquisition and LabVIEW software after the system reaches steady state, i.e. constant readings of temperature with small oscillations. The experiments were conducted by keeping the flow rate constant and increasing the heating power gradually. The data were recorded for 2 min at a frequency of 1 Hz and then were averaged to be used in the data reduction process.

3. Data reduction

For single phase flow, the net pressure drop along the micro channel ΔP_{ch} is given by:

$$\Delta P_{ch} = \Delta P_m - \Delta P_{loss} \quad (1)$$

where ΔP_m is the total measured pressure drop and ΔP_{loss} is the total pressure losses due to the pressure drop in inlet manifold

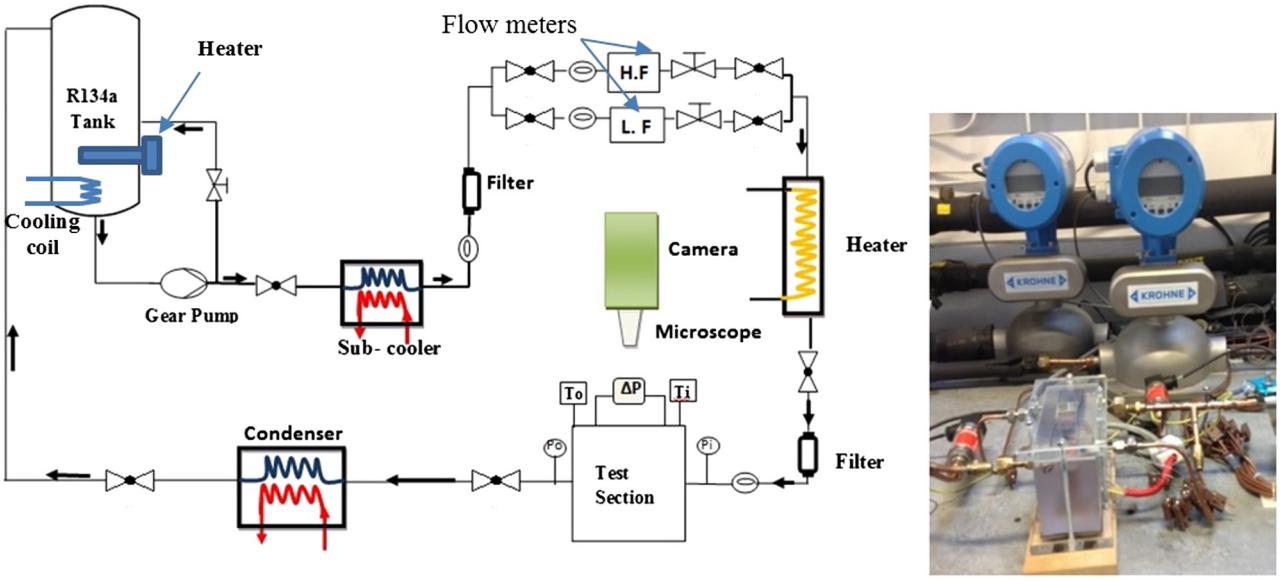

Fig. 1. Schematic drawing of the test loop and closed-up photograph of the test section.

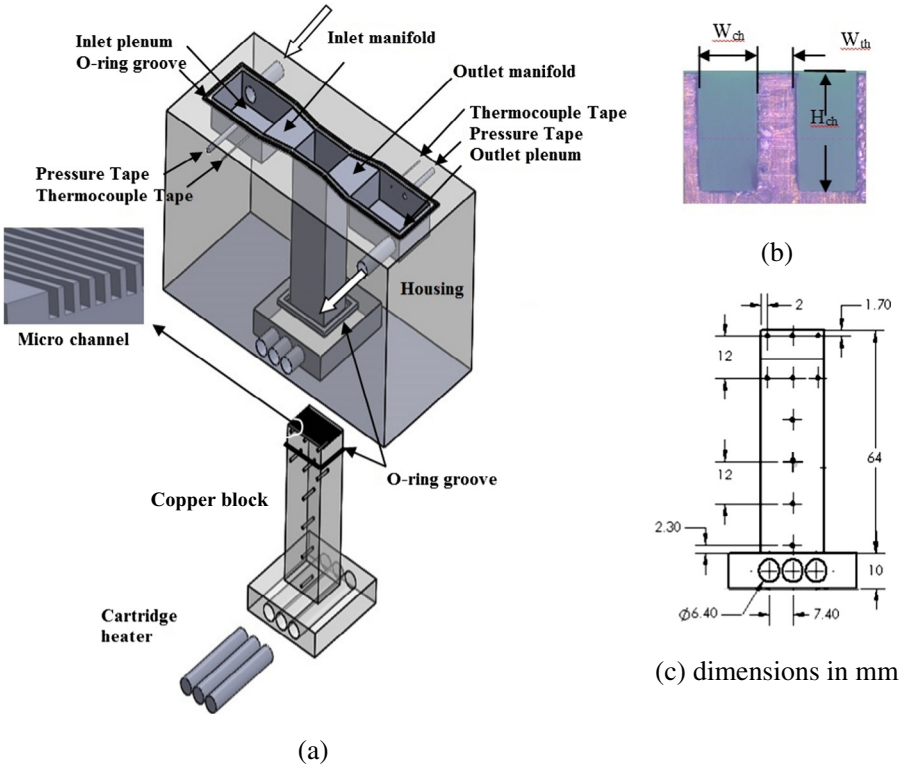

Fig. 2. (a) Test section, (b) microscopic picture of microchannel, and (c) dimensions of copper block.

ΔP_{mi}, outlet manifold ΔP_{mo}, sudden contraction ΔP_{sc}, and sudden expansion ΔP_{ex}, see Eq. (2) below.

$$\Delta P_{loss} = \Delta P_{mi} + \Delta P_{sc} + \Delta P_{ex} + \Delta P_{mo} \tag{2}$$

The pressure losses in the above equation are given below, see Remsburg [16].

$$\Delta P_{mi} = [1 - \beta^2 + K_{mi}] \times \frac{1}{2} G^2 v_f \tag{3}$$

$$\Delta P_{mo} = -\left[\frac{1}{\beta^2} - 1 + K_{mo}\right] \times \frac{1}{2} G^2 v_f \tag{4}$$

The loss coefficients K_{mi} and K_{mo} depend on the manifold convergence and divergence angle θ and the values are summarized in the textbook given by Shaughnessy et al. [17] in a table format as a function of the area ratio β and angle θ. The values are 0.134 for K_{mi} and 0.11 for K_{mo} for our design. In the above equations β is the small to large cross sectional area ratio, G is the mass flux and v_f is the liquid specific volume. The mass flux is calculated using Eq. (5) below.

$$G = \frac{\dot{m}}{N(W_{ch}H_{ch})} \tag{5}$$

In the above equation, $\dot{m}$ is the total mass flow rate and N is the number of channels. The sudden contraction and expansion losses in Eq. (2) are given by the following equations, reported in Ref. [16]:

$$\Delta P_{ex} = -\left[\frac{1}{\beta^2} - 1 + (1-\beta)^2\right] \times \frac{1}{2} G^2 v_f \tag{6}$$

$$\Delta P_{sc} = [1 - \beta^2 + 0.5(1-\beta)] \times \frac{1}{2} G^2 v_f \tag{7}$$

The contribution of the losses at the highest Reynolds number (Re = 2936) due to the inlet manifold, the outlet manifold, the sudden contraction and the sudden expansion were 2.5%, 2.9%, 8.2% and 12.3%, respectively. These values will be lower for lower Reynolds number. The experimentally determined single phase fanning friction factor is then calculated as:

$$f_{\exp} = \frac{\Delta P_{ch} D_h}{2 L v_f G^2} \tag{8}$$

For two phase flow, the pressure loss due to sudden expansion ΔP_{ex} and outlet manifold ΔP_{mo} in Eq. (2) must be considered as two phase flow. The pressure loss due to the outlet manifold can be calculated using Eq. (9) below given by Liu and Groll [18].

$$\Delta P_{mo} = 0.425 G^2 (1-\beta^2) \left[\frac{x_{exit}^2}{\rho_g} + \frac{(1-x_{exit})^2}{\rho_f}\right] \tag{9}$$

The pressure loss due to the sudden expansion can be calculated using Eq. (10) given by Collier and Thome [19].

$$\Delta P_{ex} = 0.5 G^2 (1-\beta^2) v_f \left[1 + \frac{v_g - v_f}{v_f} x_{exit}\right] \tag{10}$$

where v_g is the gas specific volume. The exit vapour quality in the above equation can be calculated as:

$$x_{exit} = \frac{i_{exit} - i_f}{i_g - i_f} \tag{11}$$

where i_{exit}, i_f, i_g are the specific enthalpy of the fluid at the exit and saturated liquid and saturated vapour respectively. These parameters are estimated at the exit temperature and pressure. Since the flow enters the channel as a single phase liquid, the channel pressure drop is divided into single phase part, ΔP_{sp} and a two phase part, ΔP_{tp}. Thus, the net two phase pressure drop along the channel is calculated as:

$$\Delta P_{tp} = \Delta P_{ch} - \Delta P_{sp} \tag{12}$$

The single phase pressure drop along the single phase region can be calculated from:

$$\Delta P_{sp} = \frac{G^2 f_{sp} L_{sp}}{2 v_f D_h} \tag{13}$$

The length of the single phase region L_{sp} is calculated from an energy balance as:

$$L_{sp} = (T_{sat} - T_{f,in}) \frac{\dot{m} c_{pf}}{q'' W} \tag{14}$$

where c_{pf}, T_{sat}, $T_{f,in}$, q'', W are the liquid specific heat, saturation temperature at the location of zero vapour quality, fluid inlet temperature, base heat flux and width of the heat sink respectively. The above set of equations enabled the calculation of the local pressure at L_{sp}. The local pressure at the beginning of the boiling region was then set equal to this value. The single phase friction factor f_{sp} in Eq. (13) is the apparent friction factor and is evaluated using Eq. (15) below given by Shah and London [20] for developing flow.

$$f_{sp} Re = \frac{3.44}{\sqrt{x^+}} + \frac{K(\infty)/(4x^+) + (fRe)_{fd} - 3.44/\sqrt{x^+}}{1 + C'/(x^+)^{0.2}} \tag{15}$$

In the above equation, x^+ is the dimensionless axial distance (L/ReD_h). $(fRe)_{fd}$, while $K(\infty)$ and C' are constants that depend on the aspect ratio. For the geometry used in the present study, the values are 0.931, 0.000076 and 19.071 respectively for $K(\infty)$, C' and $(fRe)_{fd}$. The Reynolds number is calculated as GD_h/μ_f and the base heat flux q'' is calculated from the measured temperature gradient as:

$$q'' = k_c \frac{dT}{dy} \tag{16}$$

where k_c is the thermal conductivity of copper and y is the vertical distance. The local thermocouples were inserted at 1 mm distance from the channel bottom. Thus, the readings of these thermocouples ($T_{w,th}$) were corrected using the 1D heat conduction equation to obtain the temperature at the inner surface of the channel (T_w), as given by Eq. (17).

$$T_w = T_{w,th} - \frac{q'' d}{k_c} \tag{17}$$

The local heat transfer coefficient plotted in this paper was calculated at the midpoint of the heat sink using the mid thermocouple $T_{w,m}$ after correcting the reading using Eq. (17) and is given by Eq. (18). Similar calculations were performed at the other two thermocouple locations, see Fig. 2(c).

$$h = \frac{q'' W}{(T_{w,m} - T_f)(W_{ch} + 2\eta H_{ch}) N} \tag{18}$$

If the midpoint is located in the single phase region, the fluid temperature T_f is calculated using Eq. (19) below.

$$T_f = T_{f,in} + \frac{q'' W z}{\dot{m} c_{pf}} \tag{19}$$

where z is the axial distance, η is the fin efficiency ($\eta = \tanh(mH_{ch})/mH_{ch}$), m is the fin parameter $\sqrt{2h/k_c W_{th}}$. The fin efficiency was calculated with the assumption that the fin has an adiabatic tip. If the midpoint is located in the two phase region, the saturation temperature is used. This saturation temperature is obtained assuming that pressure drop varies linearly along the two phase region. This assumption was discussed in [21,22]. There is a steeper pressure drop in the nucleate boiling region at boiling incipience than the other flow regime regions of the passages. The linear assumption can result in higher pressures, hence higher saturation temperatures and as a consequence the actual heat transfer coefficient will be lower than the calculated one. The difference is probably small since the length of the nucleate region is much smaller than the regions where the other flow patterns prevail. In single passages this assumption can be removed by adding pressure taps along the passage – something of course more difficult in multichannels, see [23] by the present group. Additionally, in multi microchannels heat sinks, the channel length is very small compared to the long passages in conventional heat exchangers and thus the measured pressure drop across the microchannels is small. Accordingly, the variations in the saturation temperature along the channel will be small and the assumption of linear pressure drop will not have a significant effect. The local vapour quality is calculated as:

$$x(z) = \frac{i(z) - i_f}{i_g - i_f} \tag{20}$$

Experimental data were acquired at 6.5 bar system pressure over the following range of parameters: mass flux G = 50–300 kg/m^2 s and heat flux q'' = 11.46–403.1 kW/m^2. The propagated

uncertainty analysis was conducted using the method explained in Coleman and Steel [24] and the values were 2.5–2.39%, 2.7–3% and 14–40% respectively for heat flux, heat transfer coefficient and fanning friction factor. The higher value of the uncertainty of the friction factor (40%) is due to errors in the flow and pressure drop measurement at the lowest Reynolds number. The number of data for this low Re is small, i.e. usually the first and second data points, and does not affect the conclusion reached in this paper. It is worth mentioning that the average heat transfer coefficient presented in this paper is simply the average of the three local values. This is a reasonable and possible approach because of the small differences in the values of the heat transfer coefficient.

4. Results and discussions

4.1. Single-phase validation

Single phase experiments were conducted before boiling experiments to validate the experimental system. Fig. 3(a) depicts the measured friction factor compared with the Shah and London [20] correlation for developing flow (Eq. (15)) and fully developed flow ($f = C/Re$). The constant C is 19.071 for the geometry used in the present study. The figure demonstrates that there is a good agreement with the correlations and the deviation is within the experimental uncertainty. Fig. 3(b) shows the experimental Nusselt number ($Nu_{exp} = hD_h/k_f$) compared with the predictions from the correlations of Shah and London [20] and Stephan and Preuber [25] defined below by Eqs. (21) and (22), respectively. It is obvious that the experimental values show a similar trend, i.e. the Nusselt number increases with Reynolds number but the values are much higher than the predictions from the two correlations. Note that the correlations of Shah and London and Stephan and Preuber were derived based on data for a single passage. However, the current experimental results agree very well with the experimental results of Agostini et al. [8] for a multi-microchannel configuration. Agostini et al. [8] investigated flow boiling of R236fa and R245fa in a silicon multi-microchannel heat sink consisting of 67 rectangular channels, 0.223 mm wide, 0.68 mm high (D_h = 0.336 mm) and 20 mm long.

$$Nu = \begin{cases} 1.953(RePr\, D_h/L)^{1/3} & (RePr\, D_h/L) \geqslant 33.3 \\ 4.364 + 0.0722 RePr\, D_h/L & (RePr\, D_h/L) \leqslant 33.3 \end{cases} \quad (21)$$

$$Nu = 4.364 + \frac{0.086(RePr\, D_h/L)^{1.33}}{1 + 0.1Pr(ReD_h/L)^{0.83}} \quad (22)$$

4.2. Flow patterns

This section presents and discusses the effect of heat and mass flux on flow boiling patterns captured at the middle of the heat sink (the centre point) for system pressure 6.5 bar. The results demonstrate, for the examined mass flux range (50–300 kg/m^2 s), that three major regimes are present, namely: bubbly, slug and annular flow with bubbly/confined bubbly as a transition regime between bubbly and slug flow. Fig. 4 depicts the observed flow patterns for a mass flux value of 50 kg/m^2 s as a function of the base heat flux. At low heat flux (16.6 kW/m^2), small bubbles were observed in most channels with the majority of bubbles nucleating near the channel corners, see Fig. 4(a). These bubbles detached from the wall and moved downstream with a very low chance of coalescence. The average bubble diameter was estimated using the software of the high speed camera, which can measure the distance in pixels between two points. As seen in Fig. 4a, most bubbles have an ellipsoidal shape. Thus, the length of the axis of the bubble in the axial flow direction (L_{ba}) and in the transverse direction (L_{bt}) was measured (see the schematic drawing in Fig. 4f). The equivalent spherical bubble diameter can be calculated using Eq. (23) below.

$$D_{eq} = \sqrt[3]{L_{ba}^2 L_{bt}} \quad (23)$$

The equivalent diameter is defined as the diameter of a sphere that has an equivalent volume of the ellipsoidal shape. On doing so, the equivalent average bubble diameter in Fig. 4a ranged from 90.2 to 112.7 μm (0.21D_h to 0.27D_h) and the length of the bubble in the transverse direction was about 0.35 times the channel width (W_{ch}). In other words, the bubble size is much smaller than the size of the channel. As the heat flux increased to 28 kW/m^2 (Fig. 4b), the equivalent average bubble diameter increased moderately in most channels and ranged from 91.4 to 157.7 μm (0.22D_h to 0.38D_h) and thus the flow regime is still bubbly flow. The length of the bubble in the transverse direction ranged from 0.33W_{ch} to 0.53W_{ch}, i.e. it does not reach the confinement size. It is worth noting that, at this heat flux, some bubbles were observed nucleating on top of the

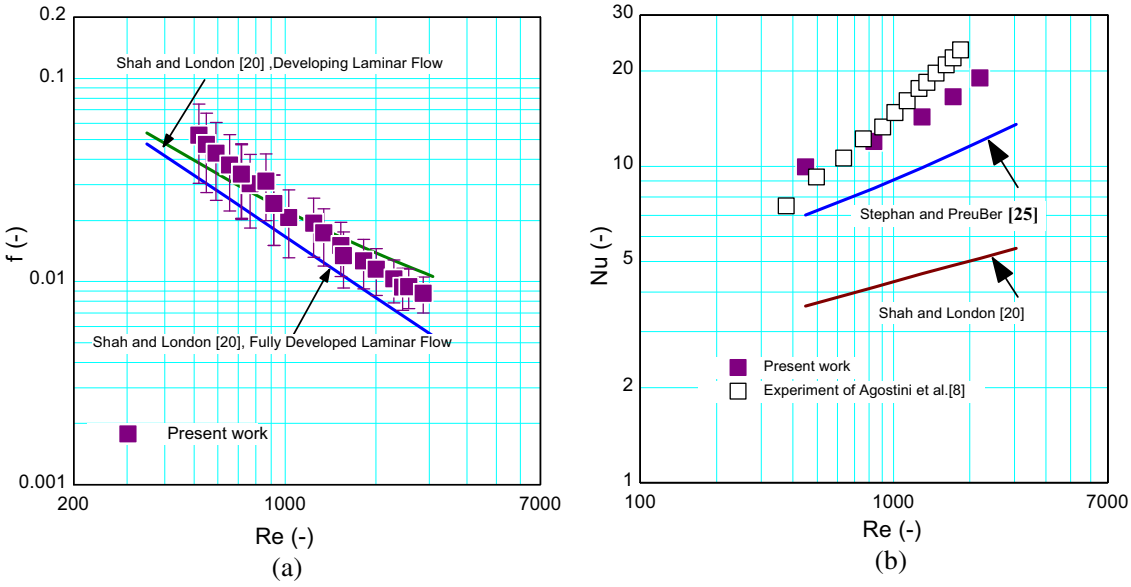

Fig. 3. Single phase results (a) fanning friction factor versus Reynolds number (b) Nusselt number versus Reynolds number.

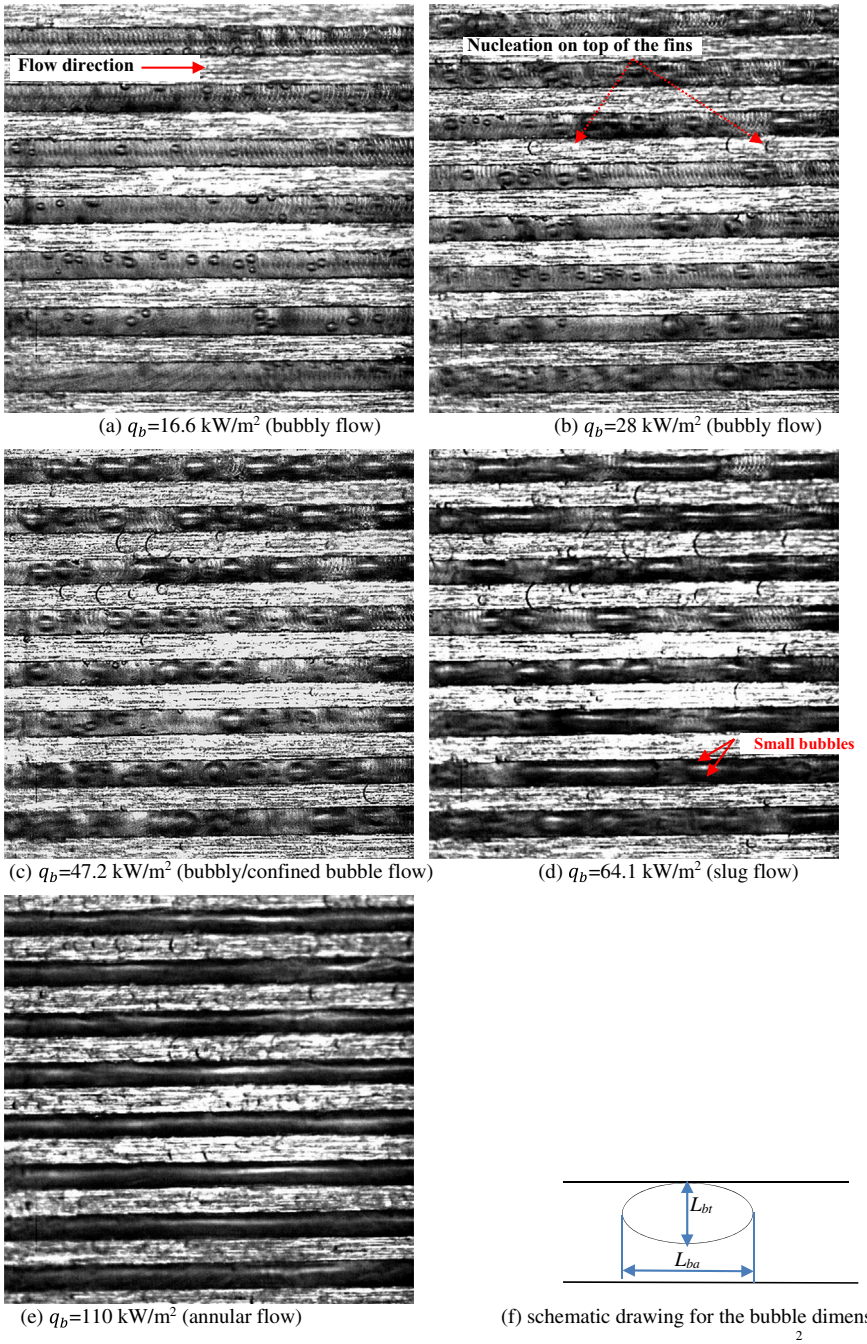

(a) q_b=16.6 kW/m^2 (bubbly flow)

(b) q_b=28 kW/m^2 (bubbly flow)

(c) q_b=47.2 kW/m^2 (bubbly/confined bubble flow)

(d) q_b=64.1 kW/m^2 (slug flow)

(e) q_b=110 kW/m^2 (annular flow)

(f) schematic drawing for the bubble dimensions

Fig. 4. Flow boiling patterns as a function of heat flux at G = 50 kg/m^2 s.

separating walls among the channels; see the arrows in Fig. 4b. This means that, the top transparent cover plate did not seal the channels completely and there is a tiny clearance between the top surface of the channels and the top plate. The number of these bubbles is small and they do not contribute to the subsequent slug formation or to the heat transfer rates to any significant amount. As the heat flux increased to 47.16 kW/m^2 (Fig. 4(c)), the bubble growth and coalescence rate increased and some channels exhibited confined bubble flow, where bubble size is such that it spans the channel width, while bubble coalescence was observed in some other channels. The equivalent average bubble diameter ranged from 139 to 290 μm (0.33D_h to 0.7D_h) and the bubble length in the transverse direction ranged from 144 to 277 μm (0.48W_{ch} to 0.93W_{ch}). Increasing the heat flux to 64.1 kW/m^2 (Fig. 4(d)) resulted in slug flow in most channels. In this regime, small nucleating bubbles are still observed in the liquid slug and near the channel walls, see the arrows in Fig. 4d. With further increase in heat flux to 110 kW/m^2, the flow exhibits features of annular flow, see Fig. 4(e). In this regime, the vapour flows in the core of the channel with a wavy nature and it can touch the side walls of the channels periodically. The nucleation on top of the separating walls was also observed in annular flow. The same flow patterns were also observed for mass fluxes 100, 200, 300 kg/m^2 s. It is worth mentioning that nucleation in the liquid film in annular flow was also observed at higher heat flux (152.1 kW/m^2) for G = 100 kg/m^2 s, see Fig. 5.

4.3. Bubble nucleation

This section presents and discusses some features of nucleation in microchannels for G = 50–300 kg/m^2 s. The pictures presented in this section were captured at the middle location of the heat sink (the centre point). The focus will be only on a single active nucleation site in one of the channels at very low heat fluxes in order to avoid the interaction among the nucleation sites occurring at relatively higher heat fluxes due to the activation of more sites. Fig. 6 depicts the effect of heat flux on bubble departure diameter (D_{eq}), bubble departure time (t_d) and the waiting time (t_w) for G = 50 kg/m^2 s as a function of heat flux. The bubble departure diameter is measured at the moment when the bubble is about to leave the nucleation site. The departure time t_d (bubble growth time) is defined as the time it takes for the bubble to grow before leaving the nucleation site. The waiting time t_w is defined as the time between the departure of the bubble and the appearance of the next bubble at the same nucleation site. Fig. 6 shows that as the heat flux increases, the bubble growth rate increases and the bubble growth time decreases. At q = 16.6 kW/m^2, the equivalent bubble departure diameter was 55 μm, the bubble growth time was 7 ms and the waiting time was about 2 ms. This means that bubble generation frequency ($1/(t_w + t_d)$) at this heat flux was 125 bubbles per second. During the bubble growth time, the bubble diameter increased by 79%, i.e. from the time it was possible to record by the camera to departure. At q = 21.6 kW/m^2, the equivalent bubble departure diameter increased to 67.5 μm, the bubble growth time decreased to 5 ms, the waiting time 2 ms and the bubble generation frequency increased to 143 bubbles per second. The bubble diameter increased by 74% during the bubble growth time. Increasing the heat flux further to 28 kW/m^2 resulted in the following: the bubble departure diameter increased to 76.2 μm, the bubble growth time decreased to 3 ms, the waiting time 2 ms and the bubble generation frequency increased to 200 bubbles per second. The bubble diameter increased by 132% during the bubble growth time. Fig. 6 demonstrates also that the bubble does not depart towards the centre of the channel after it leaves the nucleation site. Instead, the bubble slides on the side wall at the channel corner for a short distance before it moves to the centre of the channel. It is interesting to note that when the bubble departure diameter was calculated using Eq. (24) below given by Cole and Rohsenow [26], the value was 62.9 μm for R134a at 6.5 bar.

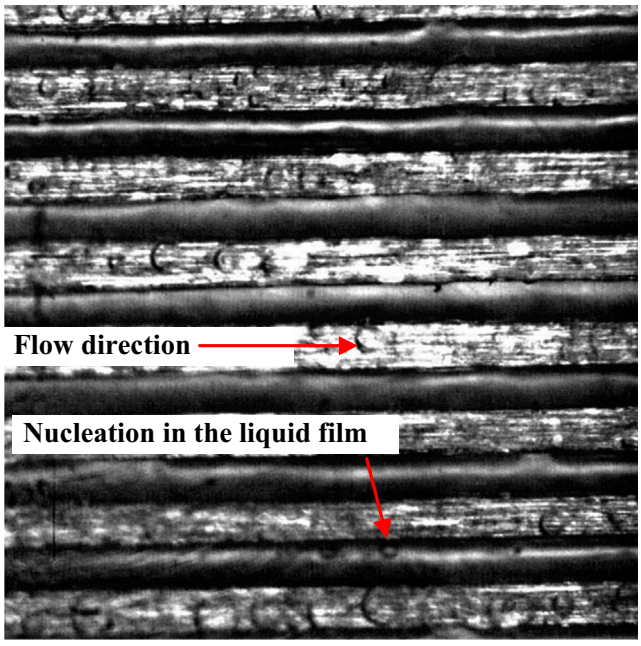

Fig. 5. Nucleation in the liquid film in annular flow for G = 100 kg/m^2 s and q = 152.1 kW/m^2.

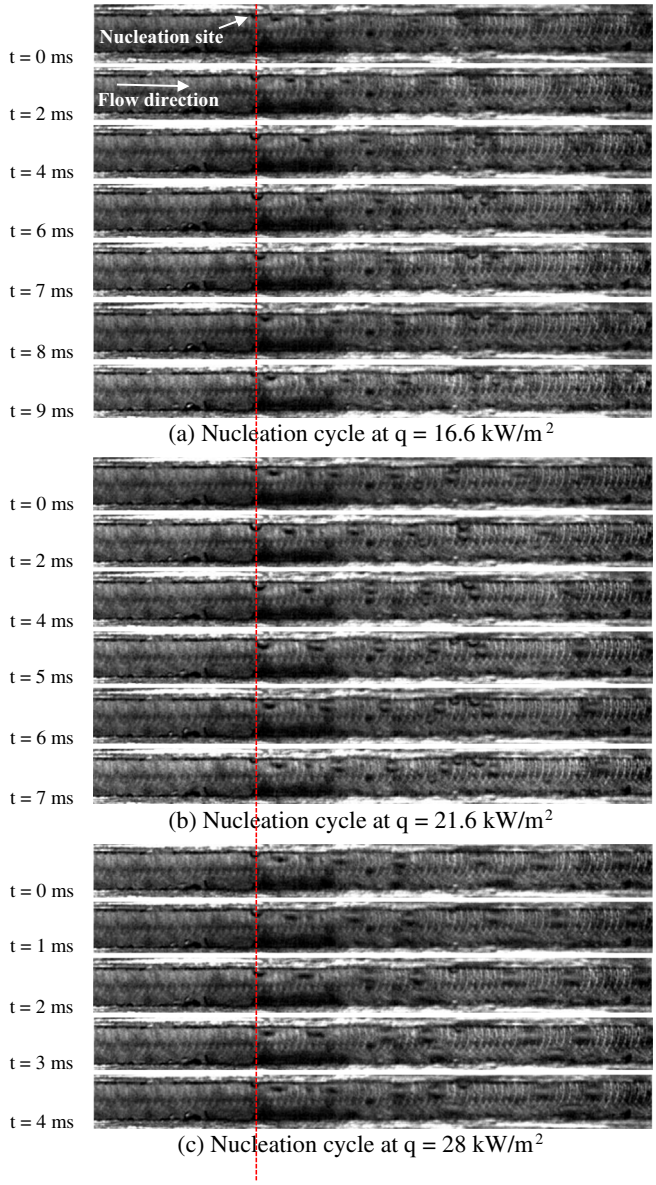

Fig. 6. Effect of heat flux on bubble nucleation cycle at G = 50 kg/m^2 s.

$$D_b = 0.000465 Ja^{1.25} \sqrt{\frac{\sigma}{g(\rho_f - \rho_g)}} \tag{24}$$

$$Ja = \frac{c_{pf}\rho_f T_{sat}}{\rho_g h_{fg}} \tag{25}$$

This equation takes into account the saturation temperature, fluid properties (liquid and vapour density, liquid specific heat, latent heat and surface tension) and gravity and surface tension forces. The predicted value is in rough agreement with the measured bubble departure diameter which ranged from 55 to 76.2 μm. The deviation could be due to the possible periodic variation in the mass flux within the channel and the fact that the correlation does not take the effect of inertia into account. In order to have an insight in the mass flux within the channel, the bubble velocity was measured immediately after departure from the nucleation site. The bubble velocity could be an indicator of the

mass flux within the channel provided that there is no slip between the liquid and vapour phases, i.e. the liquid and vapour flow with the same velocity. This assumption is reasonable at very low vapour quality, which is the case in our current discussion. The velocity was measured by measuring the distance travelled by the bubble over a time interval. On doing so, the bubble velocity ranged from 0.056 m/s to 0.067 m/s for q = 16.6 kW/m^2, which corresponds to a single channel mass flux range 67.7–78.8 kg/m^2 s (the nominal mass flux value was 50 kg/m^2 s). The variation in the mass flux within the channel could be resulting from the difference in nucleation characteristics from one channel to another which leads to a variation in the pressure drop along each channel. The difference in pressure drop results in re-distribution of the flow among channels. In other words, the calculation of channel mass flux based on the assumption that the flow is uniformly distributed may become invalid after boiling incipience.

Owing to the fact that the flow is not uniformly distributed among the channels and thus the mass flux in the channels can vary, it is difficult to understand the effect of mass flux on nucleation using the nominal mass flux values 50–300 kg/m^2 s. Instead, the effect of mass flux on nucleation is explained herein using the mass flux within the channel calculated from the measured bubble velocity at the same heat flux. Fig. 7 depicts bubble nucleation for a nominal mass flux value of 100 kg/m^2 s at q = 28 kW/m^2. The bubble velocity was found to range from 0.023 m/s to 0.11 m/s corresponding to a channel mass flux range 27–132 kg/m^2 s. Fig. 7a indicates that when the mass flux reaches its minimum value in the channel (27 kg/m^2 s), the bubbles move very slowly and thus grow due to evaporation before the size increases further due to bubble coalescence. It is very obvious that the bubble attains a spherical shape and the bubbles depart towards the centre of the channel without a sliding motion. The measured bubble departure diameter is 51 μm and the bubble growth time is about 5 ms. At a channel mass flux value of 78 kg/m^2 s (Fig. 7b), the large bubbles started to show distortion while the bubbles near the nucleation site become elongated (ellipsoidal shape) with an equivalent bubble diameter of 33 μm. At channel mass flux value of 132 kg/m^2 s (Fig. 7c), the nucleation site acts as a vapour jet and it is difficult to measure the size of the bubbles at this condition. Form the above discussion, it is obvious that it is difficult in multi micro channel configurations to have a final conclusion on the effect of mass flux on bubble size and frequency. They both depend strongly on the distribution of the flow among the channels.

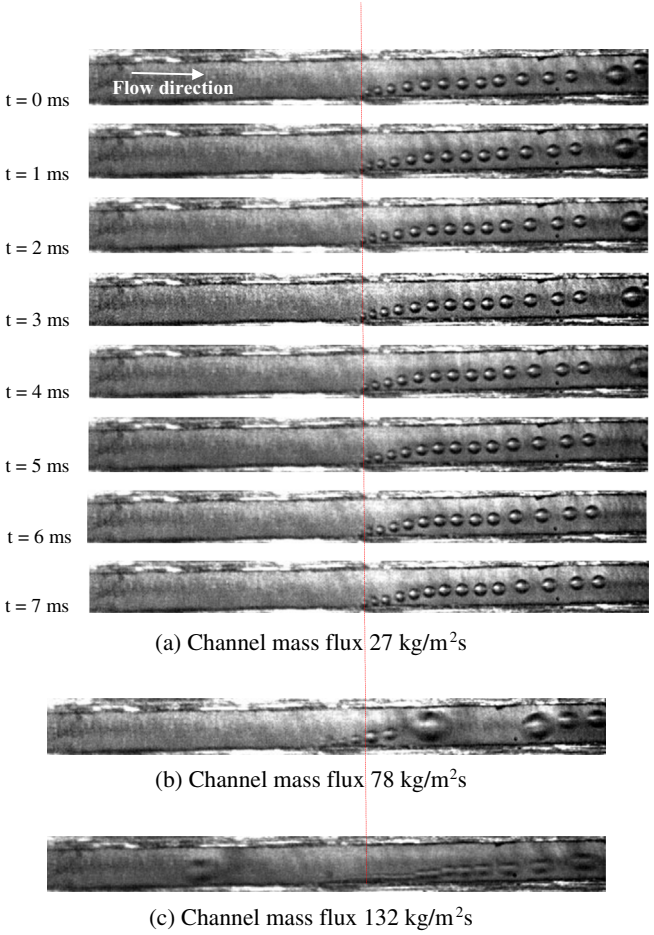

Fig. 7. Effect of channel mass flux on bubble nucleation q = 28 kW/m^2 and a nominal mass flux of 100 kg/m^2 s.

4.4. Flow reversal

A set of experiments were conducted at the same conditions (P = 6.5 bar, G = 50–300 kg/m^2 s) but the visualization was conducted along the middle of the heat sink at a location that shows the channels inlet and part of the inlet manifold in order to detect flow reversal. The results demonstrated, for the examined mass flux range, that the observed flow patterns were fluctuating between single phase liquid, bubbly and elongated bubble flow (slug flow). It was found that for G = 50 kg/m^2 s, flow reversal occurred at boiling incipience and continued for all heat flux values. Fig. 8 shows the sequence of pictures for flow reversal occurring at boiling incipience for P = 6.5 bar and G = 50 kg/m^2 s. It is obvious from the pictures that the vapour patch stays for about 210 ms in the inlet manifold with back and forth motion before its rupture into segmented bubbles that moved to the downstream side. As the mass flux was increased, the heat flux at which flow reversal occurs increased. Very mild flow reversal was observed in the inlet manifold at a base heat flux value of 149 kW/m^2 for G = 300 kg/m^2 s where the vapour patch stayed only about 10 ms in the inlet manifold. Fig. 8 did not show nucleation in the channels and the vapour patches seem coming from the side channels of the heat sink (not shown in the field of view of the camera). It is important to bear in mind that the field of view of the camera is 4 × 4 mm at resolution 512 × 512 pixels. For a given mass flux, more nucleation sites become active and flow reversal is clearly observed as the heat flux increases. For example, at q'' = 84 kW/m^2, the bubbles grow to the channel size and coalesce to form vapour slugs, which exhibit periodic back and forth motion (the period was about 65 ms for this heat flux), see Fig. 9. The expansion of the bubble in both upstream and downstream directions is not observed in the present study. Bubble expansion in both directions observed by [27,28] may be specific for water not refrigerants. Flow boiling studies using water in micro channels indicated that the bubble can stay for a long time on the nucleation site and expand significantly in both directions. The bubble can stay at the generation location for more than 410 ms without departure, see for example Bogojevic et al. [29]. Accordingly, the back and forth motion observed in the present study may be attributed to the significant variations in channel pressure drop, which is related to the channel flow patterns. If the pressure drop is very high in some channels or if the local pressure increased suddenly (negative pressure drop), flow reversal will occur due to the redistribution of the flow among the channels. Khovalyg et al. [30] investigated the interactions between parallel channels during flow boiling of R134a. They conducted the test in four single channels connected in parallel having a square cross section 0.538 × 0.538 mm. Each channel has a separate preheating section in order to control the inlet vapour quality and the pressure drop was measured across each channel. The channels were transparent and coated with a

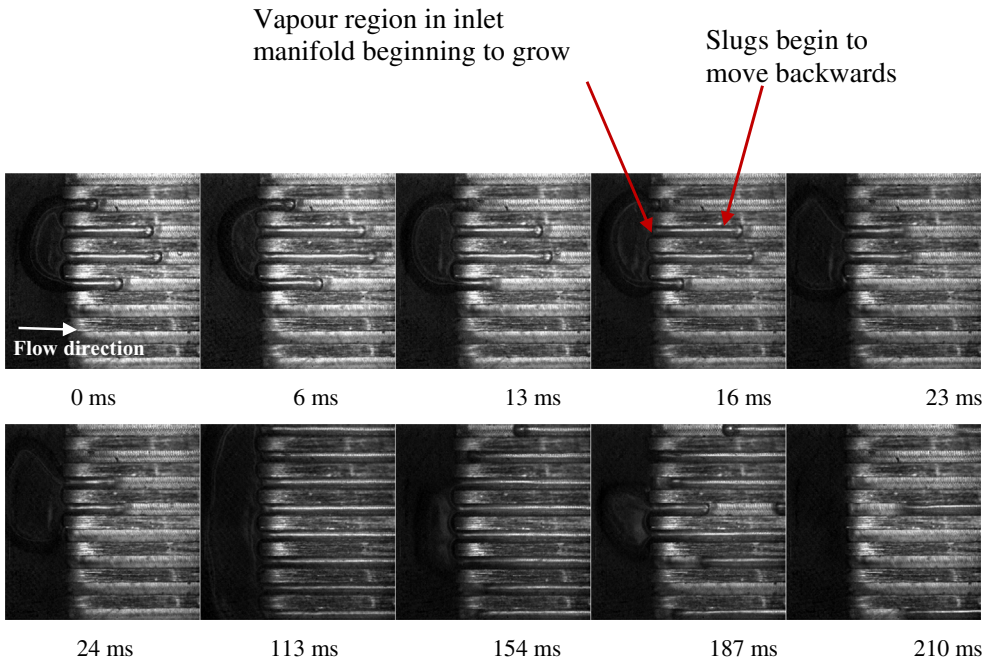

Fig. 8. Sequence of pictures for flow reversal observed at G = 50 kg/m^2 s, P = 6.5 bar and R134a.

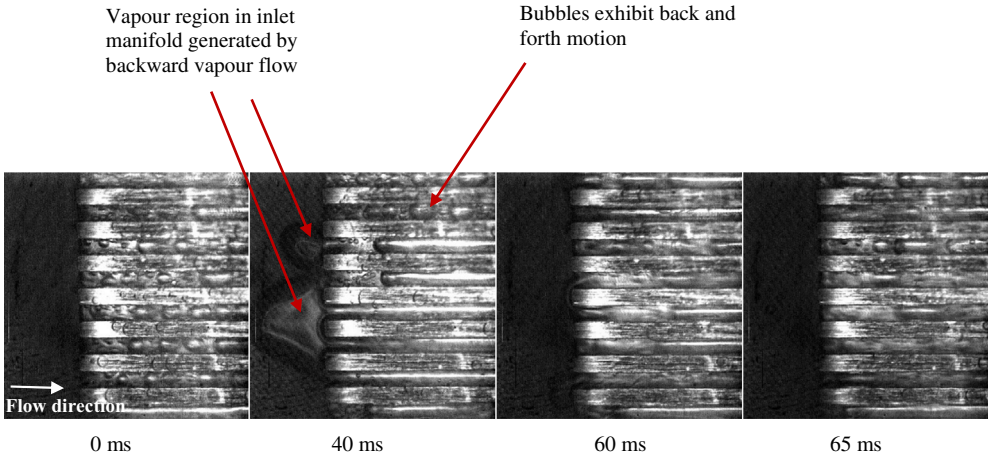

Fig. 9. Sequence of pictures for flow reversal at G = 50 kg/m^2 s and q = 84 kW/m^2.

Tungsten film such that it can be heated. The test was conducted when one channel was heated (boiling in one channel) while the other channels were in single phase flow. They reported that boiling in a single channel affected the flow distribution and pressure drop in the other channels.

It is worth mentioning that although flow reversal was observed in the present study, the recorded pressure and temperature signals did not show significant fluctuations. For example, for the flow reversal reported in Fig. 8, the maximum deviation from the mean value was 1.7% for pressure drop, 1.1% for the inlet temperature, 0.15% for the outlet temperature and 0.13% for the wall temperature. These fluctuations are small and thus the heat transfer data presented in the next section are not affected significantly by the reverse flow, i.e. the data are for stable flow.

4.5. Heat transfer results

In flow boiling studies with long test sections, it is very common to plot the local heat transfer coefficient versus local vapour quality. This was possible by measuring the local temperature at several axial locations using thermocouples. On the contrary, in multi-microchannel configurations, the channel length is very small (10–20 mm) and it would be difficult to fabricate a multi-microchannel heat sink with several drills to insert the thermocouples at several axial locations. This can be done only with a large number of integrated temperature sensors, which is very hard to be fabricated with metallic channels. Accordingly, most flow boiling studies in multi-microchannel configurations present the data in the form of the classic pool boiling curve or heat transfer coefficient at one location versus heat flux or vapour quality at this location, see the studies summarized in Table 1. The same approach is adopted here in the present paper where the results are presented as boiling curve or heat transfer coefficient versus heat flux or vapour quality at one location.

Fig. 10 illustrates the effect of mass flux on the boiling curve plotted based on the temperature measured by the thermocouple located near the channel inlet, at the middle of the heat sink and near the channel outlet. As seen in the figure, there is no

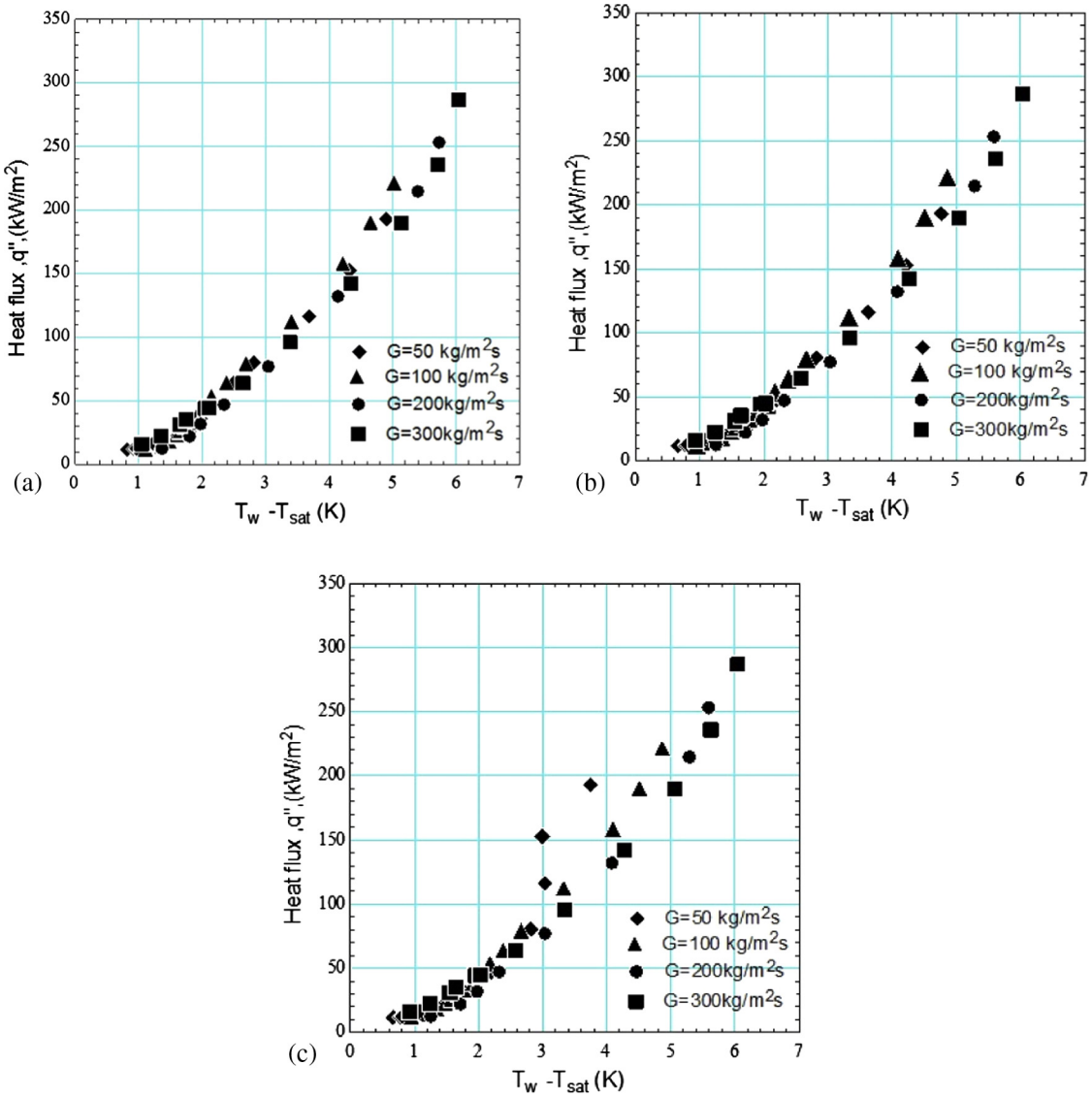

Fig. 10. Boiling curve at four different mass fluxes: (a) thermocouple location at 2 mm from the channel inlet, (b) thermocouple location at the middle, (c) thermocouple location at 2 mm from the channel outlet.

temperature overshoot for all mass fluxes and boiling started smoothly at very low wall superheat (0.8–1.2 K). The temperature overshoot depends on fluid properties and surface microstructure. For smooth surfaces and high surface tension fluids, high wall superheat will be required to start boiling, i.e. high temperature overshoot. In the present study, the Ra = 0.301 μm and R134a has small surface tension compared to other refrigerants and water. Thus, it is expected that a small wall superheat is required at boiling incipience. In order to justify this deduction, the well-known nucleation criterion given by Hsu [31] was applied using the measured Ra value in the present study. The predicted wall superheat is 1.6 K, which is in a reasonable agreement with the abovementioned value measured in the present study. The figure indicates that the heat flux increased almost linearly with wall superheat and the wall superheat at a heat flux value of 250 kW/m^2 is about 5.2 K. It is worth mentioning that this experiment was not planned to reach critical heat flux. Additionally, it is obvious from the figure that there is no clear mass flux effect on the boiling curve.

Fig. 11 illustrates the effect of heat flux, mass flux and vapour quality on the two phase heat transfer coefficient. The heat transfer coefficient in this figure is calculated at one location at the middle of the heat sink. It is obvious from Fig. 11(a) that the heat transfer coefficient increases with heat flux and does not depend on mass flux. Fig. 11(b) depicts the heat transfer coefficient versus vapour quality for different mass flux. The figure indicates that the heat transfer coefficient increases with vapour quality and mass flux, which contradicts the conclusion that one can reach if only Fig. 11(a) is assessed. This arises from the fact that, at one location, it is difficult to let one variable vary and keep the other variables fixed. For example, in Fig. 11(a), when the mass flux varies for a fixed heat flux, the vapour quality also varies. For a fixed heat flux, the vapour quality at a specific location decreases as the mass flux increases. Similarly, in Fig. 11(b), for a fixed vapour quality, the heat flux varies also with mass flux. Thus, the effect of mass flux cannot be deduced from this figure because the vapour quality and heat also varies with varying mass flux. Accordingly, the data in Fig. 11 are summarized in Table 2 for G = 50–300 kg/m^2 s to show that the vapour quality varies in Fig. 11(a) and the heat flux varies in Fig. 11(b). The results of Fig. 11 make inferring the dominant heat transfer mechanism using the conventional criteria very

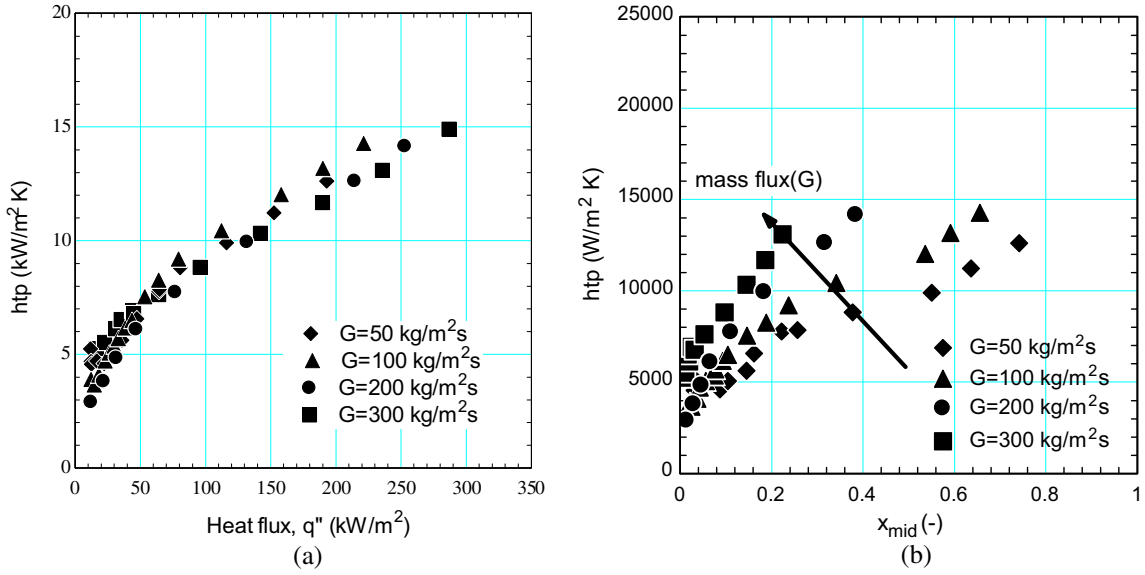

Fig. 11. Heat transfer coefficient at the middle location of the microchannel heat sink versus (a) heat flux, (b) vapour quality at the middle location.

difficult. Fig. 11(a) indicates that nucleate boiling dominates, while Fig. 11(b) indicates dominance of convective boiling. However, flow visualization demonstrated that bubble nucleation was observed up to intermediate heat flux values (q_b = 64.1 kW/m^2), i.e. bubbly and slug flow. The complex effect of mass flux in this study could be attributed to the large variations in channel mass flux as previously discussed. In other words, the results may differ if the actual channel mass flux was used rather than the mass flux calculated based on the assumption that the flow is uniformly distributed. Bertsch et al. [3] investigated flow boiling of R134a in a copper multi micro channel evaporator having hydraulic diameter 1.09 mm over a mass flux range 20.3–81 kg/m^2 s and reported similar behaviour. They reported that there is no mass flux effect on the boiling curve which agrees with the results of the present study. When the average heat transfer coefficient in their study was plotted versus exit vapour quality, a clear mass flux effect was reported and the average heat transfer coefficient increased with increasing exit quality and mass flux. Plotting the same data against heat flux indicated that the heat transfer coefficient increases with increasing heat flux but the mass flux effect was very small. In fact, the heat transfer coefficient decreases slightly with increasing mass flux, [3].

5. Comparison with exiting prediction methods

The measured heat transfer coefficient in the present work is compared with the heat transfer coefficient predicted by the correlations summarized in Table 3. We have compared in detail past correlations and published extensively on this, see [32]-where we compared with 21 correlations. We continue to compare with a significant number of correlations proposed in the past. However, in this paper, there is no intention to compare with all existing correlations and only, some correlations were selected to compare with the current data. Extensive comparison with existing state-of-the-art correlations will be conducted later when more data are collected for wide experimental ranges and different fluids. The accuracy of each correlation is estimated using the mean absolute error percentage (*MAEP*) as follows:

$$MAEP = \frac{1}{N}\sum\left|\frac{h_{exp} - h_{pred}}{h_{exp}}\right| * 100 \quad (26)$$

As shown in Fig. 12, the correlations of Lazarek and Black [33] and Kew and Cornwell [34] predicted the experimental data reasonably well at low heat and mass fluxes but the prediction gets worse as mass and heat flux increase. Tran et al. [35] modified the correlation of Lazarek and Black [33] by replacing the liquid Reynolds number with the Weber number. This correlation slightly under predicted the experimental data – but still within the ±30% error band with a mean absolute error of 27.6%. Warrier et al. [36] proposed a heat transfer correlation for micro channels which includes the effect of boiling number and vapour quality. As seen in Fig. 12(d), this correlation shows scattered data with a mean absolute value of 53%. The correlations of Cooper [37] and Mahmoud and Karayiannis [32] show the best predictions with a mean absolute error less than 20%. It is worth mentioning that the correlation of Mahmoud and Karayiannis was developed for mini/micro tubes using R134a data based on the model of Chen [38]. They modified the nucleate boiling suppression factor and the convective boiling enhancement factor and also used the Cooper [37] correlation for the nucleate pool boiling part. This correlation takes into account also the effect of channel diameter, which is embedded in the enhancement factor. The similarity in performance between this correlation and Cooper correlation and the agreement with the experimental data means that the correlation can predict the dominant mechanism well. In other words, the correlation predicts that there is suppression for the convective boiling enhancement factor. The agreement with the Cooper correlation may be considered as an indication of the existence of nucleate boiling heat transfer mechanism for a significant range in this study. However, this requires further investigation.

6. Conclusions

Flow boiling experiments in a copper multi microchannel heat sink using R134a were performed for a mass flux range 50–300 kg/m^2 s and heat flux range 11.46–403.1 kW/m^2. Flow boiling patterns were also studied using a high-speed high-resolution camera. The main concluding points can be summarized as follows:

1. Three flow patterns were observed when the heat flux was increased gradually in small steps. These patterns include bubbly, slug and wavy-annular flows. Bubble nucleation was also observed in the liquid film in slug flow and wavy-annular flow.

Table 2
Data used in Fig. 11 for G = 50–300 kg/m^2 s.

G [kg/m^{2}s]	q'' [W/m^2]	T_{sat} [°C]	h_{exp} [W/m^2 K]	Vapour quality [–]
50	11,458	24.30	5240	0.0290
	11,973	24.30	4699	0.0424
	12,171	24.34	4549	0.0315
	16,571	24.32	4722	0.0450
	22,040	24.30	4610	0.0865
	28,737	24.26	5050	0.1039
	35,592	24.42	5621	0.1448
	47,162	24.45	6569	0.1617
	64,078	24.66	7778	0.2214
	64,591	24.81	7837	0.2567
	80,407	24.21	8822	0.3776
	116,060	24.03	9889	0.5506
	152,484	24.57	11,235	0.6355
	192,821	24.95	12,611	0.7415
100	12,131	24.30	3886	0.0211
	14,549	24.30	3658	0.0250
	17,997	24.32	4088	0.0376
	22,832	24.28	4711	0.0433
	26,082	24.35	5053	0.0559
	29,648	24.40	5359	0.0760
	32,818	24.47	5695	0.0765
	38,404	24.64	6155	0.0931
	43,593	24.77	6492	0.1043
	53,309	24.12	7531	0.1461
	63,969	24.01	8265	0.1879
	79,223	24.05	9191	0.2371
	112,142	24.07	10,441	0.3412
	158,044	24.21	12,020	0.5358
	189,912	24.56	13,169	0.5907
	221,173	25.09	14,265	0.6555
200	12,130	24.40	2906	0.0141
	21,641	24.43	3820	0.0292
	31,547	24.59	4839	0.0474
	46,608	24.26	6114	0.0667
	76,675	24.48	7743	0.1116
	131,656	24.24	9947	0.1841
	214,818	24.06	12,620	0.3146
	214,381	24.11	12,623	0.3168
	252,980	24.31	14,154	0.3843
300	16,016	24.36	5250	0.0071
	22,438	24.07	5514	0.0110
	31,036	24.50	6122	0.0192
	35,038	24.49	6525	0.0163
	44,112	24.49	6930	0.0253
	44,745	24.51	6783	0.0315
	63,920	24.59	7626	0.0527
	95,773	24.24	8820	0.0970
	142,185	24.46	10,316	0.1453
	189,732	24.65	11,676	0.1863
	235,655	24.67	13,096	0.2234

Table 3
Flow boiling heat transfer correlations used for the comparison with experimental data.

Lazarek and Black [33]	$h_{tp} = 30\frac{k_l}{D_h}Re_l^{0.857}Bo^{0.714}$, $Bo = q''/Gh_{fg}$, $Re_l = \frac{D_h G(1-xe)}{\mu_l}$
Cooper [37]	$h_{tp} = 55\, P_R^{(0.12-0.2\log_{10}R_P)}(-\log_{10}P_R)^{-0.55}M^{-0.5}q''^{0.67}$
Tran et al. [35]	$h_{tp} = 840000(Bo^2We_l)^{0.3}\left(\frac{\rho_l}{\rho_g}\right)^{-0.4}$
Kew and Cornwell [34]	$h_{tp} = 30\frac{k_l}{D_h}Re_l^{0.857}Bo^{0.714}(1-xe)^{-0.143}$
Warrier et al. [36]	$h_{tp} = Eh_l$, $h_l = Nu_4\frac{k_l}{D_h}$, $E = 1 + 6Bo^{1/16} - 5.3(1-855Bo)xe^{0.65}$
	$Nu_4 = 8.235\left(1 - 2.042\beta + 3.767\beta^2 - 2.477\beta^3 + 5.361\beta^4 - 0.1865\beta^5\right)$
Mahmoud and Karayiannis[32]	$h_{tp} = (Eh_l + Sh_{nb})$, $h_l = 4.36\frac{k_l}{D_h}$ *for* $Re_l < 2000$
	$h_l = 0.023\, Re_l^{0.8}Pr_l^{0.4}\frac{k_l}{D_h}$ *for* $Re_l > 3000$, $E = \left[1 + \frac{A}{X_{tt}}\right]^{0.64}$,
	$S = \frac{1}{1+2.56*10^{-6}(Re_lE^{1.25})^{1.17}}$
	$Re_l = \frac{D_h G(1-xe)}{\mu_l}$
	$A = 2.812\ Co^{-0.408}$

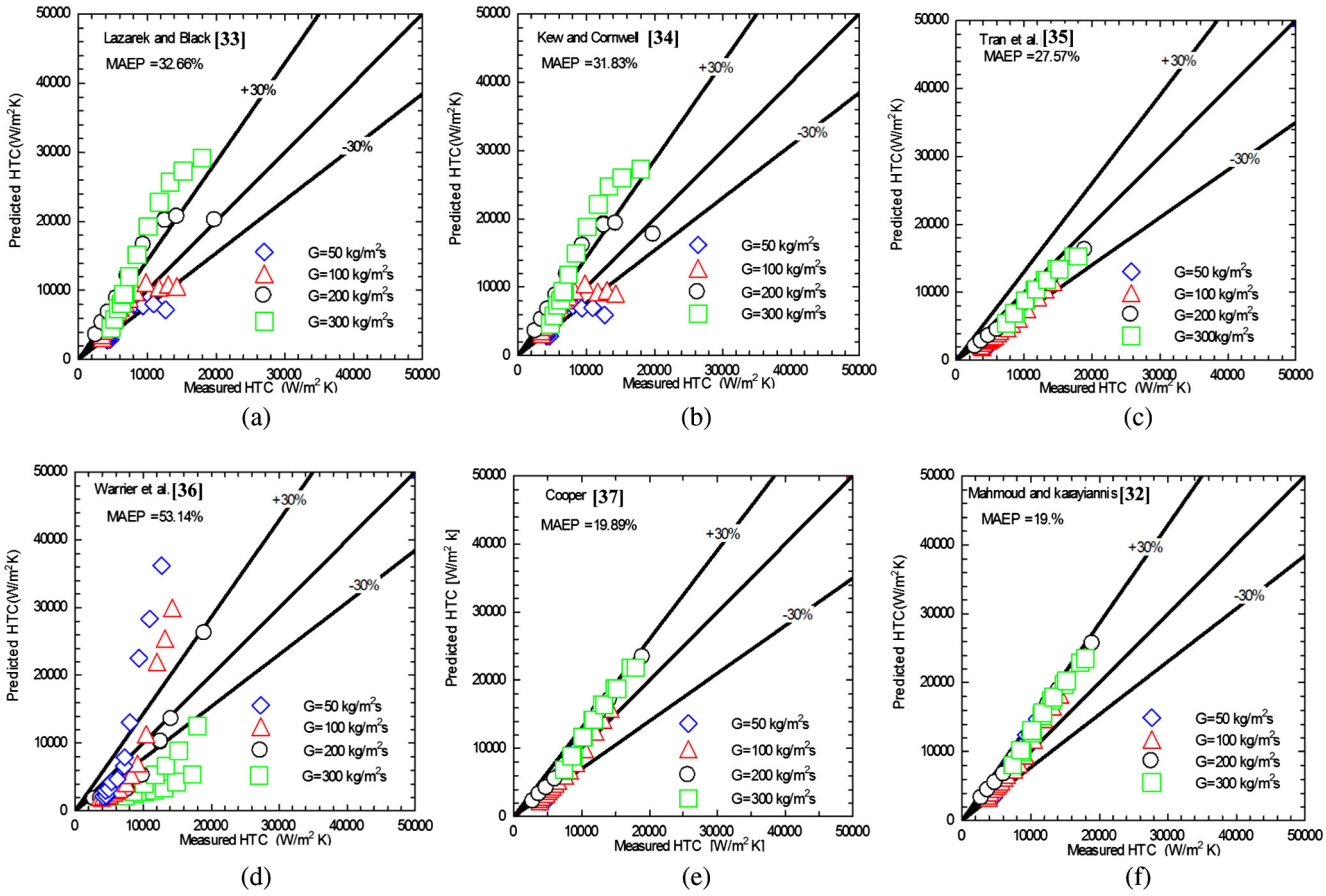

Fig. 12. Comparison of the measured boiling heat transfer coefficient with existing correlations.

2. The bubble departure diameter and frequency were found to increase as the heat flux increases. This was based on a close observation of one nucleation site. Also, the bubble departure diameter decreases as the mass flux increases.
3. The fundamental study of nucleation characteristics in multi-channels is not easy and can produce varying results due to variations in the mass flux in each channel, which in turn affects the nucleation process and subsequently the prevailing heat transfer mechanism(s). Therefore, using the mass flux effect to infer the mechanism may not be appropriate in multichannels.
4. Flow reversal is very evident for the lowest mass flux (50 kg/m^2 s) at all heat flux values. As the mass flux increased from 100 to 300 kg/m^2 s, the heat flux at which flow reversal occurs increased. An in depth evaluation study of flow reversal and flow instabilities is recommended. Such a study should include their effect on heat transfer rates. Despite the flow reversal, the recorded pressure and temperature signals exhibited insignificant fluctuations.
5. The heat transfer results demonstrated that the heat transfer coefficient depends strongly on heat flux while it is a week function of mass flux. However, plotting the heat transfer coefficient versus vapour quality indicated dependence on vapour quality and mass flux. Based on that, it would be difficult to infer the dominant mechanism using the conventional criteria. This behaviour could be specific for multi-channel configurations compared to single channels due to the significant variations in flow distribution (mass flux) among the channels.
6. Comparison with existing macro and micro scale correlations demonstrated that only the correlations of Mahmoud and Karayiannis [32] and Cooper [37] predicted the experimental data very well with a mean absolute error less than 20%.

The correlation of Mahmoud and Karayiannis is recommended for design purposes, although further research and comparisons are also advisable, because this correlation was developed for single tubes.

References

[1] I. Mudawar, Two phase microchannel heat sinks: theory, applications and limitations, J. Electron. Packag. 133 (041002) (2011) 1–31.
[2] T. Chen, S.V. Garimella, Measurement and high speed visualization of flow boiling of a dielectric fluid in a silicon micro-channel heat sink, Int. J. Multiphase Flow 32 (8) (2006) 957–971.
[3] S.S. Bertsch, E.A. Groll, S.V. Garimella, Refrigerant flow boiling heat transfer in parallel micro-channels as a function of local vapour quality, Int. J. Heat Mass Transfer 51 (2008) 4775–4787.
[4] S.S. Bertsch, E.A. Groll, S.V. Garimella, Effect of heat, mass flux, vapour quality, and saturation temperature on flow boiling heat transfer in microchannels, Int. J. Multiphase Flow 35 (2009) 142–154.
[5] Y. Madhour, J. Olivier, E.C. Patry, S. Paredes, B. Michle, J.R. Thome, Flow boiling of R134a in a multi-micro channel heat sink with hotspot heaters for energy – efficient microelectronic CPU cooling application, IEEE Trans. Compon. Pack. Manuf. Technol. 1 (2011) 873–883.
[6] H.L. Leao, S.L. Nascimento, F.J. Do, G. Ribatski, Flow boiling heat transfer of R407C in a microchannels based heat spreader, J. Exp. Therm. Fluid Sci. 59 (2014) 140–151.
[7] W. Qu, I. Mudawar, Flow boiling heat transfer in two phase micro-channel heat sink – Part I. Experimental investigation and assessment of correlation method, Int. J. Heat Mass Transfer 46 (2003) 2755–2771.
[8] B. Agostini, J.R. Thome, M. Fabbri, B. Michel, D. Calm, U. Kloter, High heat flux flow boiling in silicon multi-microchannels – Part I: Heat transfer characteristics of refrigerant R236fa, Int. J. Heat Mass Transfer 51 (2008) 5400–5414.
[9] S. Mortada, A. Zoughaib, C.A. Daurelle, Boiling heat transfer and pressure drop of R-134a and R-1234yf in minichannels for low mass fluxes, Int. J. Refrig. 35 (2012) 962–973.
[10] J. Lee, I. Mudawar, Two phase flow in High heat flux micro-channel heat sink for refrigeration cooling applications: Part II – Heat transfer characteristics, Int. J. Heat Mass Transfer 48 (2005) 941–955.

[11] T. Harirchian, S.V. Garimella, Microchannel size effects on local flow boiling heat transfer to a dielectric fluid, Int. J. Heat Mass Transfer 51 (2008) 3724–3733.
[12] P.S. Lee, S.V. Garimella, Saturated flow boiling heat transfer and pressure drop in silicon microchannel arrays, Int. J. Heat Mass Transfer 51 (2008) 789–806.
[13] K. Balasubramanian, M. Jagirdar, P.S. Lee, C.J. Teo, S.K. Chou, Experimental Investigation of flow boiling heat transfer and instabilities in straight microchannels, Int. J. Heat Mass Transfer 66 (2013) 655–671.
[14] T.G. Karayiannis, M.M. Mahmoud, D.B.R. Kenning, A study of discrepancies in flow boiling results in small to microdiameter metallic tubes, Exp. Therm. Fluid Sci. 36 (2012) 126–142.
[15] T. Harirchian, S.V. Garimella, Effect of channel dimension, heat flux, and mass flux on flow boiling regimes in microchannels, Int. J. Multiphase Flow 35 (2009) 349–362.
[16] R. Remsburg, Thermal Design of Electronic Equipment, CRC Press, 2000.
[17] E.J. Shaughnessy, I.M. Katz, J.P. Schaffer, Introduction to Fluid Mechanics, Oxford University Press, New York, Oxford, 2005.
[18] F. Liu, E.A. Groll, Analysis of a two phase flow ejector for the transcritical CO_2 cycle, in: Int. Refrigeration and Air Conditioning Conference at Purdue, July 14–17, 2008.
[19] J.G. Collier, J.R. Thome, Convective Boiling and Condensation, third ed., Oxford University Press, Oxford, UK, 1994.
[20] R.K. Shah, A.L. London, Laminar flow forced convection in ducts. Suppl. 1, Adv. Heat Transfer, 1978.
[21] P.A. Kew, K. Cornwell, On pressure fluctuations during boiling in narrow channels, in: 2nd European Thermal Sciences Conference, Rome, 1996, pp. 1323–1329.
[22] S. Lin, P.A. Kew, K. Cornwell, Two-phase heat transfer to a refrigerant in a 1 mm diameter tube, Int. J. Refrig. 24 (2001) 51–56.
[23] S. Gedupudi, Y.Q. Zu, T.G. Karayiannis, D.B.R. Kenning, Y.Y. Yan, Confined bubble growth during flow boiling in a mini/micro-channel of rectangular cross-section. Part I: Experiments and 1-D modelling, Int. J. Therm. Sci. 50 (3) (2011) 250–266.
[24] H.W. Coleman, W.G. Steele, Experimentation and Uncertainty Analysis Forengineers, second ed., John Wiley and Sons Inc, New York, 1999.
[25] K. Stephan, P. Preußer, Wärmeübergang und maximale wärmstromichte beim behältersieden binärer und ternärer flüssigkeitsgemische, Chem. Ing. Tech. 51 (1979) 37.
[26] R. Cole, W.M. Rohsenow, Correlation of bubble departure diameter for boiling of saturated liquids, AIChE Chemmical Engineering Progress Symposium Series, vol. 65, 1969, pp. 211–213.
[27] G. Wang, P. Cheng, H. Wu, Unstable and stable flow boiling in parallel microchannels and in a single microchannel, Int. J. Heat Mass Transfer 50 (2007) 4297–4310.
[28] E. Galvis, R. Culham, Measurements and flow patterns visualization of two-phase flow boiling in single channel microevaporator, Int. J. Multiphase Flow 42 (2012) 52–61.
[29] D. Bogojevic, K. Sefiane, G. Durusma, A.J. Walton, Bubble dynamics and flow boiling instabilities in microchannels, Int. J. Heat Mass Transfer 58 (2013) 663–675.
[30] D.M. Khovalyg, P.S. Hrnjak, A.V. Baranenko, A.M. Jacobi, Interactions between parallel minichannels during flow boiling of R134a, in: Proceedings of the ASME 2014 12th Int. Conf. on Nanochannels, Microchannels, and Minichannels, ICNMM2014, August 3–7, 2014, Chicago, USA.
[31] Y.Y. Hsu, On the size range of active nucleation cavities on a heating surface, J. Heat Transfer 84 (1962) 207–216.
[32] M.M. Mahmoud, T.G. Karayiannis, Heat transfer correlation for flow boiling in small to micro tubes, Int. J. Heat Mass Transfer 66 (2013) 553–574.
[33] G.M. Lazarek, S.H. Black, Evaporative heat transfer, pressure drop and critical heat flux in a small tube with R113, Int. J. Heat Mass Transfer 25 (1982) 945–960.
[34] P.A. Kew, K. Cornwell, Correlations for the prediction of boiling heat transfer in small diameter channels, Appl. Therm. Eng. 17 (8–10) (1997) 705–715.
[35] T.N. Tran, M.W. Wambsganss, D.M. France, Small circular and rectangular channel boiling with two refrigerants, Int. J. Multiphase Flow 22 (1996) 485–493.
[36] G.R. Warrier, V.K. Dhir, L.A. Momoda, Heat transfer and pressure drop in narrow rectangular channels, Exp. Therm. Fluid Sci. 26 (2002) 53–64.
[37] M.G. Cooper, Saturation nucleate pool boiling, in: 1st UK National Conference on Heat Transfer, vol. 2, 1984, pp. 785–793 (Industrial and Chemical Engineering Symposium Series No. 86).
[38] J.C. Chen, A correlation for flow boiling heat transfer to saturated fluids in convective flow, Ind. Eng. Chem. Process Des. Dev. 5 (3) (1966) 322–329.